EARLY ONLINE RELEASE

This is a preliminary PDF of the author-produced manuscript that has been peer-reviewed and accepted for publication. Since it is being posted so soon after acceptance, it has not yet been copyedited, formatted, or processed by AMS Publications. This preliminary version of the manuscript may be downloaded, distributed, and cited, but please be aware that there will be visual differences and possibly some content differences between this version and the final published version.

Evaluating cloud frequency of occurrence and top height using space-borne lidar observations

MAIKE AHLGRIMM *

COLORADO STATE UNIVERSITY, FORT COLLINS, COLORADO

DAVID A. RANDALL

COLORADO STATE UNIVERSITY, FORT COLLINS, COLORADO

MARTIN KÖHLER

EUROPEAN CENTRE FOR MEDIUM-RANGE WEATHER FORECASTS

READING, ENGLAND

June 1, 2009

Corresponding author address: MAIKE AHLGRIMM, EUROPEAN CENTRE FOR MEDIUM-RANGE WEATHER FORECASTS, SHINFIELD PARK, READING RG2 9AX, UNITED KINGDOM

E-MAIL: MAIKE.AHLGRIMM@ECMWF.INT

Abstract

A strategy for model evaluation using space-borne lidar observations is presented. Observations from the Geoscience Laser Altimeter System are recast onto the model grid in order to assess the ability of two versions of the Integrated Forecasting System to model marine stratocumulus clouds. The two model versions differ primarily in their treatment of clear and cloudy boundary layers. For each grid column, a representative cloud fraction and cloud-top height are derived from the observations, as well as from the model. By applying the same threshold critera for cloud fraction and top height independently to model and observations, samples containing marine statocumulus clouds can be identified. The frequency of occurrence, cloud fraction and cloud-top height distributions for all samples thus identified are compared.

The evaluation shows improvements in the frequency of occurrence and top height of marine stratocumulus, though modeled cloud tops remain lower than observed. Additional runs reveal a sensitivity to the strength of the environmental mixing that occurs during the test parcel ascent of the boundary layer parameterization. With a more agressive parcel, the modeled clouds agree even better with observations.

1. Introduction

Observations from space-borne lidar provide a novel perspective on clouds. The lidar is able to directly measure the height of multiple cloud layers, provided the upper layers are not optically thick. A variety of studies have examined overlap statistics (Wang and Dessler 2006), distributions of cloud-top and base heights (Hart et al. 2005; Dessler et al. 2006b) and the occurrence and backscatter properties of optically thin clouds (Dessler et al. 2006a). There are also studies that show the value of these observations for model evaluation. Miller et al. (1999) use a threat score analysis to test how well the model's cloud fields match observations in time and space. In Palm et al. (2005), a comparison with lidar observations shows an overestimation of high cloud amount in the ECMWF model. Wilkinson et al. (2008) also evaluate the ECMWF model by comparing zonally averaged frequency of occurrence and amount of clouds. A lidar forward model is used in this case to account for signal attenuation.

These previous model evaluations have examined overall cloudiness of the model, averaging in time and space to obtain meaningful statistics. In this article, a different approach is followed. Using observations from the Geoscience Laser Altimeter System (GLAS), we focus on one cloud type, marine stratocumulus (MSc), and compare the frequency of occurrence, typical cloud fraction and cloud top height for this cloud type. Marine stratocumulus is a good cloud-type candidate for several reasons: MSc exist in areas of subsidence with little upper cloudiness to fully attenuate the lidar signal. The MSc clouds themselves have a very strong backscatter signal, which is unlike the weaker signal of near-surface aerosol layers. The large signal-to-noise ratio of the clouds' backscatter gives greater confidence in the re-

3

trieved cloud-top height. A major drawback is the accompanying rapid signal attenuation, usually before the cloud base can be detected. Thus, the cloud base height is not considered in this study. The large horizontal extent and persistence of MSc clouds means they are frequently observed by the lidar and individual observations are likely to be similar to the time and space average of the observations. Last but not least, MSc clouds play an important role in the Earth's radiative balance and many models, including the ECMWF model, do not generate the right amount of MSc with the observed properties (Bretherton et al. 2004; Duynkerke and Teixeira 2001; Zeng et al. 2004). Thus, the choice of cloud type capitalizes on the strengths of the lidar observing system, manages to avoid some of its limitations and addresses an area of interest in cloud modeling.

By focusing on one cloud type, instead of global cloud occurrence, observed characteristics of the cloud type can be compared to the equivalent clouds in the model. Systematic errors highlight specific deficiencies and point the way for targeted improvement of parameterizations.

Section 2 will briefly introduce the GLAS data products and the examined model versions. In section 3, the methods for identification of MSc samples are explained. Results of the evaluation are discussed in section 4 and section 5 concludes this article.

2. Observations and Model

a. Observational Data

The lidar observations used here are from the Geoscience Laser Altimeter System (GLAS) on board the Ice, Cloud and Land Elevation Satellite (ICESat). The cloud layer product (GLA09) at 5 Hz from laser period 2A (26 September 2003 to 18 November 2003) is used (Zwally et al. 2003). Local overpasses occur twice daily around 7:00 and 19:00 local time near the Equator. Both day and nighttime retrievals are used. The lidar's nominal vertical resolution is approximately 76.8 m and the layer product is based on observations from the green channel (532 nm). The pulse frequency is 40 Hz. Eight backscatter profiles are averaged before processing in the 5 Hz products, which corresponds to an along-track resolution of about 1400 m. The averaged profile is searched from the top down for consecutive vertical bins with backscatter exceeding a threshold. Up to ten cloud-top and -base height pairs are saved in the GLA09 product (Brenner et al. 2003). Figure 1, panel a), shows the attenuated backscatter of a daytime GLAS track in the south east Pacific. Photons from sunlight scattered into the beam lead to a noisy background. Nonetheless, the stratocumulus clouds have a very clear signal about an order of magnitude larger than the background noise. The lidar beam is quickly attenuated in most shots. Panel b) shows the cloud boundaries from the level 2 product. Retrieved cloud tops and bases are connected by a black line, whereas the grey lines indicate an attenuated profile below the apparent cloud base. A profile is considered fully attenuated when no ground return signal can be found.

b. Model

Two model cycles, CY28R3 (operational from 28 September 2004 to 18 October 2004) and CY29R1 (operational from 5 April 2005 to 28 June 2005), of the ECMWF's Integrated Forecasting System (IFS) are evaluated. The IFS is initialized at noon every other day from the operational analysis and run at T511L60 resolution (approximately 40 km grid spacing) for three days. Three-hourly output from forecast hours 12 to 57 is remapped onto a $1° \times 1°$ regular latitude-longitude grid using nearest-neighbor sampling.

While none of the forecast cycles are identical to the analysis cycle used to initialize the forecasts, the boundary layer structure in the regions considered stabilizes within the first 12 hours of the forecast. In Fig. 2, profiles of specific humidity and potential temperature are shown at various forecast hours. In order to remove day-to-day variability, profiles from a $10° \times 10°$ degree area in the south-east Pacific are averaged together, and all 28 three-day forecast are composited. The humidity profile of the analysis [thick grey curve panels a) and b] shows that the boundary layer is less well mixed in the analysis than in any of the subsequent forecast hours shown. Plotted as thin lines are forecast hours 12 through 72 in twelve-hour increments. Forecasts verifying at 00 UTC are shown as thin black lines in panels a) and c), those verifying at 12 UTC in panels b) and d). While there is a difference between day and night time, composite profiles from subsequent forecast days verifying at the same time of day fall almost on top of each other, thus showing no further drift of the boundary layer structure after forecast hour 12. For reference, the one standard deviation range at forecast hour 12 is shown as the light grey bar in the background. There is some evidence that the free atmosphere above the inversion warms and dries with forecast length,

but this appears to have little influence on the moisture and temperature profiles below. Figures are only shown for CY29R1 here, but all other cycles spin up equally quickly.

The model cycles differ primarily in their treatment of the clear and cloudy boundary layer: In CY28R3, the boundary layer is parameterized based on a K-diffusion model using dry variables (Beljaars and Viterbo 1998). All boundary layer clouds are generated either directly by the large scale cloud scheme or indirectly by the shallow convection parameterization, which provides a source term for the cloud scheme (Tiedtke 1989, 1993). In CY29R1, the Eddy Diffusivity Mass Flux (EDMF) framework, adapted to the dry boundary layer and stratocumulus, is introduced. It consists of a diffusive and a mass flux component and uses moist-conserved variables. This enables the scheme to represent local mixing as well as non-local transport due to large eddies. The formulation in moist-conserved variables also allows mixing through the cloud base in stratocumulus situations. The EDMF parameterization is described in detail in Tompkins et al. (2004). Aspects of the scheme relevant for this study are described in more detail below.

3. Method

The goal of the method described in this section is to identify one value each for cloud fraction and cloud-top height representative of the boundary layer (BL) clouds in each model column. Since marine stratocumulus clouds are the subject of investigation, we assume that only one layer of BL clouds exists in the lowest 2.5 km of the atmosphere. However, multiple cloud layers can exist within the column. The method outlined below may seem unnecessarily complicated, but it guarantees that the cloud top height value is truly representative of the

7

BL clouds only. A simple average of the lowest detected cloud layer could, for example, average together non-overlapping BL and mid-level clouds and thus produce an average height that is representative of neither cloud feature. The following process aims to include all detected cloud tops associated with the BL cloud feature in the grid box area, but exclude any cloud tops in the column that belong to cloud layers above the BL.

The lidar tracks are co-located in space and time with the nearest three-hourly gridded model data from the IFS. Hence, the observations are never more than 1.5 hours removed from the model data. The co-location procedure is loosely based on the method introduced by Miller et al. (1999). In the horizontal, each lidar shot is associated with the grid point whose $1° × 1°$ area the shot falls into.

In order to calculate a cloud fraction on vertical levels from the lidar observations, we must decide for each shot whether it is clear or cloudy on a particular model level. In the left column of Fig. 3, this decision process is shown schematically. Panel a) shows the model grid, dashed lines marking layer interfaces, overlaid on top of the lidar shots. Each black solid line connects a detected lidar cloud top and base pair. Since the lidar cloud tops and bases do not necessarily line up with the layer interfaces, the vertical extent of the clouds is rounded up or down. In this example, shot 2 fills layer 2 completely in the vertical, but layer 1 only partially. Since the shot extends more than halfway into layer 1, the shot is considered to be cloudy in this layer, as indicated by the gray shading in panel b). In contrast, shot 7 also partially extends into layer 1, but less than halfway through the depth of the layer. In this case the shot is considered to be clear in layer 1 (no gray shading). For very thin clouds, such as shots 6 and 14, the layer in which the cloud occupies the most space is considered to be cloudy - layer 2 in both examples. The grey shading in panel b) illustrates

8

the lidar-derived cloud fraction on each of the model levels using this method.

The average cloud-top height (CTH) for all clouds associated with an individual model layer is defined as the top height average of all shots considered to be cloudy in the layer. As shown in panel c), only the shots that contribute to the cloud fraction in layer 2, marked by grey shading, contribute to the CTH in that layer, calculated as the average of the tops marked with black dots. The average CTH for layer 2 is indicated in the figure. A corresponding average CTH is calculated for all model layers. Each layer's cloud fraction and CTH are checked against the critical values of 80% and 2.5 km to determine whether the column contains stratocumulus clouds. If several layers meet both criteria, the layer with the greatest cloud fraction is chosen to be most representative of the BL cloud feature, as the greatest number of lidar shots has contributed to the average CTH.

The process for deriving a corresponding cloud fraction and CTH from the model is illustrated in the right column of Fig. 3. In panel d), the model's cloud fraction is shown. The cloud fraction, indicated by the width of the grey bars, is chosen to be similar to the example in the left column. The same overlap assumption as used in the radiation scheme of the IFS (Räisänen et al. 2004) is used here to generate clear or cloudy subcolumns [panel e)]. The boundaries, or tops and bases, of these subcolumns will always fall onto the layer interfaces, so no rounding up or down is necessary. The tops of all subcolumns that are cloudy in layer 2 (black dots) contribute to the average CTH of layer 2.

A lidar simulator based on Chiriaco et al. (2006) is used to determine the level of full signal attenuation in the model subcolumns before the steps above are carried out. This additional check ensures that BL clouds obscured by optically thick layers above are excluded from the comparison, and the cloud base is adjusted to the level of full signal attenuation within

optically thick clouds. The actual simulated backscatter is not used beyond this step. For the given circumstances, the signal from the model's BL clouds is always significantly larger than the simulated molecular backscatter such that the information put into the simulator (clear and cloudy subcolumns) corresponds exactly to the output (simulated backscatter above the background threshold). No additional information about the cloud boundaries is gained by using the backscatter instead of the cloud mask.

This method for deriving the cloud-top height and fraction of the boundary layer cloud feature in each model column allows an equitable comparison between observed and modeled clouds. In Fig. 4, an example of cloud fractions for model (top panel) and observations (bottom panel) are shown for the same track as in Fig. 1.

Two stratocumulus areas are investigated here: the south-east Pacific (30°S to 0°, 70°W to 150°W) and the north-east Pacific (15°N to 35°N, 110°W to 160°W). The southern area has substantial stratocumulus cover in all seasons, and will be the main focus of this study. The Californian stratocumulus region has a maximum cloud cover around July (Klein and Hartmann 1993). The laser 2A period in the fall is not ideal to study the norht-east Pacific region, but it is included to illustrate the model's regionally-dependent response to the sensitivity tests discussed further below.

The comparison of the lidar's along-track cloud fraction to the model's grid-box area cloud fraction presents a source of error. A satisfactory way of quantifying this error from the lidar observations alone could not be established. Astin et al. (2001) propose a statistical method to calculate error estimates for along-track cloud fraction measurements. However, their method fails in the limit of full cloud cover, as it requires a minimum number of clear and cloudy sections along the track, within the region considered. Applied to the case here,

with $1° \times 1°$ grid boxes, an average of 90 lidar shots per grid box and many observed cases of 100% cloud fraction, the method proves to be unsatisfactory. Thus, we present the along-track cloud fraction as is. Qualitatively, the results presented in the following section prove to be robust for changes of the critical cloud fraction threshold.

4. Results

a. South-East Pacific (SEP)

The total number of ocean grid points within the SEP region sampled during the laser 2A period is 12440, for model and observations both. Out of these samples, 3657 (29.4%) GLAS samples are classified as MSc. These samples occur most frequently in the eastern part of the ocean basin (Fig. 5, panel a). Figure 6 shows histograms of along-track cloud fraction [panel a)] and layer-average cloud top height [panel b)] for all GLAS samples classified as MSc. Both cloud fraction (in the case of lidar observations) and cloud top height (both lidar and model) have preferred values due to a finite number of lidar shots, vertical bins in the lidar profile, and model layers in the IFS. Bins in the cloud fraction histograms are purposely chosen large (5 %), in part to average out the preferred values of the distribution, but also to reflect the potentially large uncertainty associated with comparing along-track cloud fraction to area cloud fractions. For the cloud top height distributions, a small bin size (50 m, solid black curve) preserves more detail. For an easier comparison with observations, a boxcar running mean over three bins is also shown (thick grey curve). The cloud top height distribution from the lidar observations has a broad maximum between 1250 m and 1500 m.

This range is in good agreement with observations of the trade inversion height during the East Pacific Investigation of Climate (EPIC) made two years prior during the same season (Bretherton et al. 2004).

CY28R3 produces only 1391 samples (11.2%) fulfilling the MSc criteria, primarily located in the eastern half of the region (Fig. 5, panel b). Most samples fail the cloud fraction criteria in this cycle. Panel c) in Fig. 6 shows in particular the lack of samples with cloud fractions above 95%. BL clouds in this model version can be generated through the large scale cloud scheme or shallow convection, which acts as a source term to the large scale clouds. By keeping track of the shallow scheme's activity and monitoring cloud fraction from time step to time step, we confirm that the BL clouds in this region are generated primarily by the almost constantly active schallow convection parameterization. The parameterization is optimized for shallow cumulus clouds typically having low cloud fraction. It is not an ideal representation of the processes occurring within the well-mixed, stratocumulus-topped marine boundary layer. The cloud-top height distribution of the MSc is much lower than observed (Fig. 6, panel d) with a broad peak around 750 m.

The EDMF boundary layer scheme in CY29R1 is capable of producing stratocumulus clouds as part of the boundary layer when conditions are appropriate. The number of samples classified as MSc is 2303 (18.5%) for this cycle and the frequency of occurrence map of these samples is similar to the GLAS map [Fig. 5, panel c], a significant improvement over the previous cycle. The additional samples tend to have cloud fractions above 95%, as can be seen in Fig. 6, panel e). However, there are still more MSc observed by GLAS. The additional samples are primarily located further west in the ocean basin. Unfortunately, the cloud top height distribution shows that the majority of model samples still have significantly lower

cloud tops than observed (Fig. 5, panel f), though an improvement over the previous cycle is evident. About half of this discrepancy in cloud top height between observations and model is consistent with a lower-than-observed trade wind inversion in the IFS. A study by Hannay et al. (2009) comparing CY29R1, as well as several other models, to in-situ observations in the stratocumulus areas off the Chilean coast indicate an underestimation of the trade inversion height by roughly 200 m in the IFS, and an even greater underestimation for the other models examined. These low inversions are not specific to the IFS cycle or boundary layer scheme, but a longer-standing problem in the IFS; they also exist in CY28R3.

The introduction of the EDMF parameterization clearly improves the amount and location of MSc clouds in the model. Two sensitivity runs of CY29R1 are used to address the remaining issues of the excessively low cloud top heights and the confinement of MSc samples to the near-coastal areas.

Since the depth of the convective boundary layer is determined through test parcel ascent in the EDMF, the effect of a more aggressive test parcel on the stratocumulus cloud top height is examined. Additional motivation derives from the observation that the test parcel in the parameterization frequently fails to reach the lifting condensation level. In the parameterization, the test parcel is given a temperature and moisture excess at the surface, which is diluted through lateral entrainment of environmental air as the parcel is lifted. This entrainment term takes the form of $\varepsilon = 1/\tau w + c_\varepsilon/z$, based on large eddy simulation studies (Siebesma and Teixeira 2000; Siebesma et al. 2007). Here, τ is a timescale of 500s, w the vertical velocity, z height above ground and $c_\varepsilon = 0.55$ a constant factor. The vertical velocity w approaches zero at the top and bottom of the modeled eddy (i.e. surface and BL top) such that ε becomes infinite in the limit. The second term assures this limit at the surface,

as the vertical velocity can be non-zero in the lowest model layer. In the sensitivity test, the second term in the expression is dropped, such that $\varepsilon = 1/\tau w$. This leads to a slighly reduced lateral entrainment near the surface and hence a more energetic parcel.

The resulting more aggressive parcel ascent leads to a shift of the cloud top height distribution to higher values (Fig. 8, panel a). The peak of the cloud top height distribution is now in better agreement. MSc samples also become more numerous (2878, or 23.1%) and appear more frequently in areas further west in the region (Fig. 7, panel a).

The second sensitivity test consists of relaxing the lower-level stability criterion used to distinguish between stratocumulus and trade cumulus situations in the EDMF parameterization. This critical value limits the areas where stratocumlus clouds can be modeled by the EDMF parameterization to the near-coastal areas with high stability. An empirical relationship between seasonally averaged stratocumulus amount and lower level atmospheric stability was established by Klein and Hartmann (1993). Higher stratocumulus amount is generally associated with higher low-level stability, with a range of 14 K to 22 K for various regions and seasons (Klein and Hartmann 1993, Fig. 13). In the EDMF parameterization, a critical value of $\theta_{700hPa} - \theta_{sfc} = 20\,K$ is used. For the sensitivity test, this value is reduced to $16\,K$. However, the sample frequency of occurrence [total samples 2479 (19.9%)] and the cloud top height distribution [Fig. 7 panel b) and Fig. 8, panel b)] in the SEP region show little change compared to CY29R1.

b. North-East Pacific (NEP)

MSc samples are less frequently observed by the lidar in the NEP region (Fig. 9), as indicated by the lighter gray shading in panel a). While the stratocumulus extent peaks in the SEP during fall, it tends to be at a seasonal low in the NEP (Klein and Hartmann 1993). Out of 5668 grid columns searched, GLAS finds samples meeting the MSc criteria in 1295 (22.8 %) cases. The IFS with the EDMF parameterization (CY29R1) has a similar frequency-of-occurrence pattern [Fig. 9, panel b)], but finds only 823 (14.5 %) MSc samples. As in the SEP region, the modeled cloud tops are lower than observed [Fig. 10, panels a) and b)]. In contrast to the NEP region, the number of samples (1018 or 18.0 %) and cloud top height prove to be more sensitive to the relaxation of the lower-level stability criterion in CY29R1-S [Fig. 9panel c) and Fig. 10 panels c) and d)]. The peak of the CTH distribution shifts upward by a model level (approximately 200 m). It appears that the relaxed stability criterion allows the EDMF parameterization to generate clouds at additional grid points.

We conclude that generation of MSc clouds in the south-east Pacific is limited by the early termination of the parcel ascent. By decreasing lateral entrainment and thus preserving more of the test parcel's energy and humidity excess, both the CTH distribution and frequency of occurrence improve. In the north-east Pacific, the model proves to be more sensitive to the stability criterion. This is consistent with a generally weaker low-level stability found in the NEP region of the model compared to the SEP region during the observational period.

5. Conclusions

A method for model evaluation using space-borne lidar observations has been presented in this article. We focus on defining a cloud type and comparing the frequency and location of occurrence as well as characteristic properties of the cloud type between model and observations. In the older version of the ECMWF model (CY28R3), this comparison reveals a lack of marine stratocumulus clouds over the south-east Pacific ocean. The introduction of the EDMF parameterization focussed on stratocumulus clouds greatly improves the location and frequency of occurrence of MSc clouds, but the generated clouds are generally too low by approximately 400 m. This is consistent with, but cannot be completely accounted for by a lower-than-observed trade inversion in this region. Samples are also more closely confined to the near-coastal areas than the lidar observations indicate. The sensitivity of the cloud top height and near-coastal confinement of MSc samples is tested by modifying two aspects of the EDMF scheme: the strength of parcel dilution through entrainment of environmental air and the decoupling criterion based on lower-atmospheric stability. In the south-east Pacific, a more agressive test parcel leads to better (higher) cloud tops and a more realistic frequency of occurrence. In the north-east Pacific, where lower-level stability is weaker during this time of year, the model is more sensitive to the relaxed stability criterion, allowing the EDMF to generate clouds more often and leading to improvements in MSc sample frequency. However, it must be noted that cloud fraction and top height are only two aspects of the cloudy boundary layer, and further evaluation is required to determine whether the thermodynamic structure of the boundary layer also improves with the implemented changes.

The period during which GLAS provided good quality cloud observations was unfortu-

nately short. The instrument on CALIPSO is very similar though, and comparable cloud layer products are available for several years now. It is believed that the described analysis method is also applicable to CALIPSO data. Evaluation of trade wind cumulus based on CALIPSO observations will be subject of future work.

References

Astin, I., L. Di Girolamo, and H. van de Poll, 2001: Bayesian confidence intervals for true fractional coverage from finite transect measurements: Implications for cloud studies from space. *J. Geophys. Res.*, **106**, 17 303–17 310.

Beljaars, A. and P. Viterbo, 1998: *Role of the boundary layer in a numerical weather prediction model, in Clear and Cloudy Boundary Layers, edited by A. A. M. Holtslag and P G. Duynkerke*. Royal Netherland Academy of Arts and Sciences, 287–304 pp.

Brenner, A., et al., 2003: Geoscience Laser Altimeter System (GLAS) Algorithm Theoretical Basis Document, Version 4.1.

Bretherton, C., et al., 2004: The Epic 2001 Stratocumulus Study. *BAMS*, **85**, 967–977.

Chiriaco, M., R. Vautard, H. Chepfer, M. Haeffelin, J. Dudhia, Y. Wanherdrick, Y. Morille, and A. Protat, 2006: The Ability of MM5 to Simulate Ice Clouds: Systematic Comparison between Simulated and Measured Fluxes and Lidar/Radar Profiles at the SIRTA Atmospheric Observatory. *Mon. Wea. Rev.*, **134**, 897–918.

Dessler, A., S. Palm, W. Hart, and J. Spinhirne, 2006a: Tropopause-level thin cirrus coverage revealed by ICESat/Geoscience Laser Altimeter System. *J. Geophys. Res*, **111**, D08 203.

Dessler, A., S. Palm, and J. Spinhirne, 2006b: Tropical cloud-top height distributions revealed by the Ice, Cloud, and Land Elevation Satellite (ICESat)/Geoscience Laser Altimeter System (GLAS). *J. Geophys. Res*, **111**, D12 215.

Duynkerke, P. and J. Teixeira, 2001: Comparison of the ECMWF Reanalysis with FIRE I Observations: Diurnal Variation of Marine Stratocumulus. *J. Climate*, **14**, 1466–1478.

Hannay, C., D. Williamson, J. Hack, J. Kiehl, J. Olson, S. Klein, C. Bretherton, and M. Koehler, 2009: Evaluation of simulated Southeast Pacific Stratocumulus in the NCAR, GFDL and ECMWF Models. *J. Climate*, in press.

Hart, W., J. Spinhirne, S. Palm, and D. Hlavka, 2005: Height distribution between cloud and aerosol layers from the GLAS spaceborne lidar in the Indian Ocean region. *Geophys. Res. Lett*, **32**, L22S06.

Klein, S. and D. Hartmann, 1993: The Seasonal Cycle of Low Stratiform Clouds. *J. Climate*, **6**, 1587–1606.

Miller, S., G. Stephens, and A. Beljaars, 1999: Validation survey of the ECMWF prognostic cloud scheme using LITE. *Geophys. Res. Lett.*, **26**, 1417–1420.

Palm, S., A. Benedetti, and J. Spinhirne, 2005: Validation of ECMWF global forecast model parameters using GLAS atmospheric channel measurements. *Geophys. Res. Lett*, **32**, L22S09.

Räisänen, P., H. Barker, M. Khairoutdinov, J. Li, and D. Randall, 2004: Stochastic generation of subgrid-scale cloudy columns for large-scale models. *Quart. J. Roy. Meteor. Soc.*, **130**, 2047–2067.

Siebesma, A., P. Soares, and J. Teixeira, 2007: A combined eddy-diffusivity mass-flux approach for the convective boundary layer. *Journal of the Atmospheric Sciences*, **64**, 1230–1248.

Siebesma, A. and J. Teixeira, 2000: An advection–diffusion scheme for the convective boundary layer: Description and 1D results. *Preprints, 14th Symp. on Boundary Layers and Turbulence, Aspen, CO, Amer. Meteor. Soc*, 133–136.

Tiedtke, M., 1989: A Comprehensive Mass Flux Scheme for Cumulus Parameterization in Large-Scale Models. *Mon. Wea. Rev.*, **117**, 1779–1800.

Tiedtke, M., 1993: Representation of Clouds in Large-Scale Models. *Mon. Wea. Rev.*, **121**, 3040–3061.

Tompkins, A., et al., 2004: *Moist physical processes in the IFS: progress and plans*. European Centre for Medium-Range Weather Forecasts Technical Memo No. 452.

Wang, L. and A. Dessler, 2006: Instantaneous cloud overlap statistics in the tropical area revealed by ICESat/GLAS data. *Geophys. Res. Lett*, **33**, L15 804.

Wilkinson, J., R. Hogan, A. Illingworth, and A. Benedetti, 2008: Use of a Lidar Forward Model for Global Comparisons of Cloud Fraction between the ICESat Lidar and the ECMWF Model. *Mon. Weath. Rev. in Press.*

Zeng, X., M. Brunke, M. Zhou, C. Fairall, N. Bond, and D. Lenschow, 2004: Marine atmospheric boundary layer height over the eastern Pacific: Data analysis and model evaluation. *Journal of Climate*, **17**, 4159–4170.

Zwally, H., R. Schutz, S. Palm, W. Hart, S. Hlavka, J. Spinhirne, and E. Welton, 2003: GLAS/ICESat L2 Global Cloud Heights for Multilayer Clouds V028, 26 September to 18 November 2003, Natl. Snow and Ice Data Cent., Boulder, Colo.

21

List of Figures

3   Schematic illustrating strategy for determining a cloud top height and cloud fraction representative of the boundary layer cloud feature contained within one model grid column. The left columns refers to the method applied to the lidar observations, while the right column refers to the model.   27

4   Panel a) shows the model cloud fraction along the same section of track as shown in 1. Panel b) shows the corresponding lidar-derived cloud fraction.   28

5   Frequency of occurrence of MSc samples over the Laser 2A period in the southeast Pacific ocean. Panel a) shows results from the lidar observations, panel b) from the IFS with K-diffusion boundary layer parameterization (CY28R3) and panel c) from the IFS with EDMF parameterization (CY29R1).   29

6   The left column shows histograms of cloud fraction for all samples identified as MSc. Distributions of cloud top height are shown in the right column. The top row [panels a) and b)] show results from the lidar observations, the middle row [panels c) and d)] from IFS CY28R3 and the bottom row [panels e) and f)] from IFS CY29R1. The thin black curve shows the cloud top height distributions for a 50 m bin size. The thick grey curve is a boxcar running mean over three datapoints. The dashed grey curve in panels d) and f) is the smoothed distribution of lidar cloud tops.   30

7   Same as Fig. 5, with results from the sensitivity test with a more aggressive parcel ascent (CY29R1-E) in panel a) and sensitivity test with less restrictive stability criterion (CY29R1-S) in panel b).   31

8   As in Fig. 6. Panel a) shows results from sensitivity test with more aggressive parcel ascent (CY29R1-E) and panel b) shows results from the second sensitivity test with less restrictive stability criterion (CY29R1-S).   32

9   Frequency of occurrence of MSc samples in the north-east Pacific region. Show in panel a) are results from the observations, in panel b) from the IFS with EDMF parameterization (CY29R1) and in panel c) from the sensitivity run with relaxed lower-level stability criterion (CY29R1-S).   33

10   Cloud top height distributions in the north-east Pacific region for GLAS observations (a), the IFS with EDMF parameterization (b) and the IFS with modified parcel entrainment (c) and stability criterion (d).   34
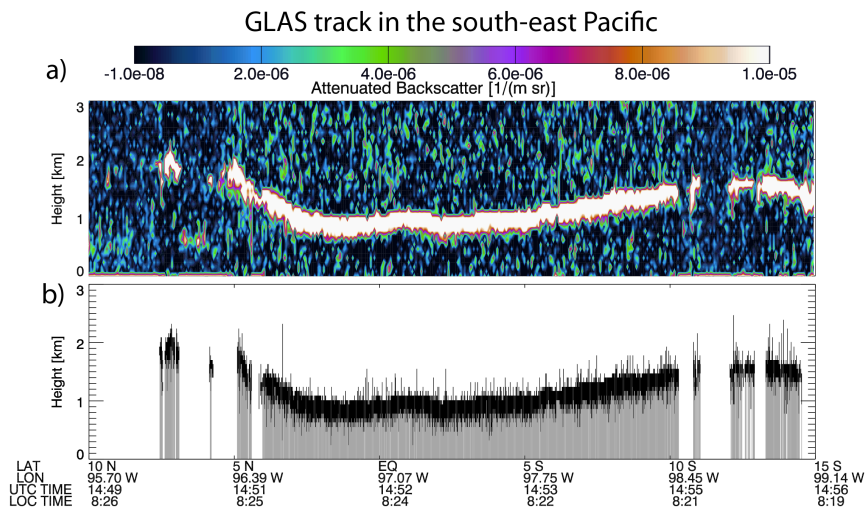
FIG. 1. Section of daytime GLAS track from 26 September 2003 between 10°N and 15°S in the south-east Pacific. Panel a) shows attenuated backscatter, panel b) shows the equivalent level 2 cloud layer product. Each detected cloud top and base pair are connected by a black line. In most cases the cloud "base" is in fact the level of full signal attenuation. Grey lines mark the attenuated shots below the level of full attenuation.
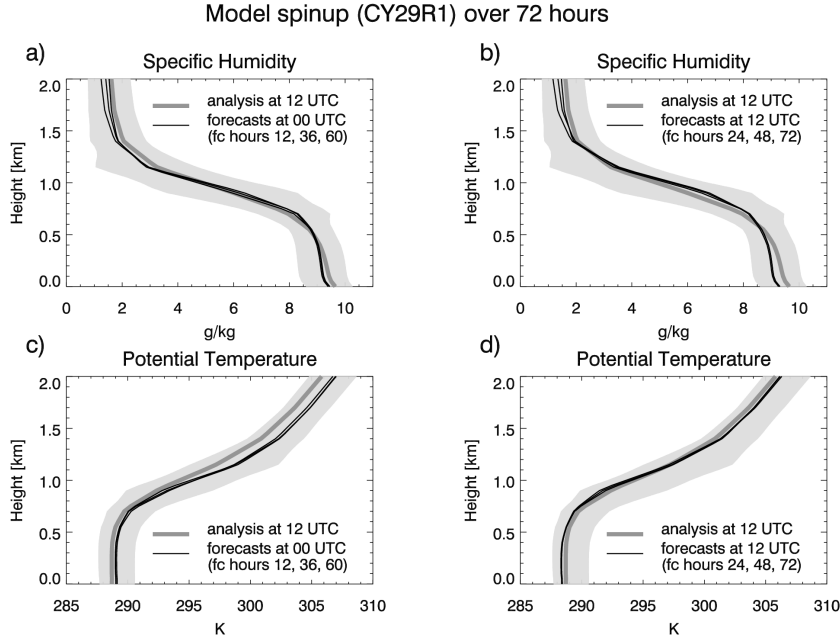
FIG. 2. Specific humidity and potential temperature profiles from CY29R1 composited over the area 15°S to 25°S, 80°W to 90°W in the south-east Pacific, and for all 28 forecasts initialized every 48 hours starting on September 25th 2003 at 12 UTC. Shown as a dark grey solid line in each of the panels is the composite profile of the analysis. Plotted as thin black lines are the composite profiles at forecast hours 12 through 72 in 12 hour steps. In panels a) and c), only the forecast hours verifying at 00 UTC are shown, wheras forecast hours verifying at 12 UTC are plotted in panels b) and d). Profiles differ between night and daytime (compare left panels to right panels), but profiles verifying at the same UTC time are almost identical in the boundary layer. That is, the boundary layer structure does not adjust significantly after forecast hour 12. There is evidence of adjustment during the first 12 hours of the forecast, as well as of a slight drift above the inversion. For comparison, the one standard deviation range at forecast hour 12 is shown as wide grey bar.
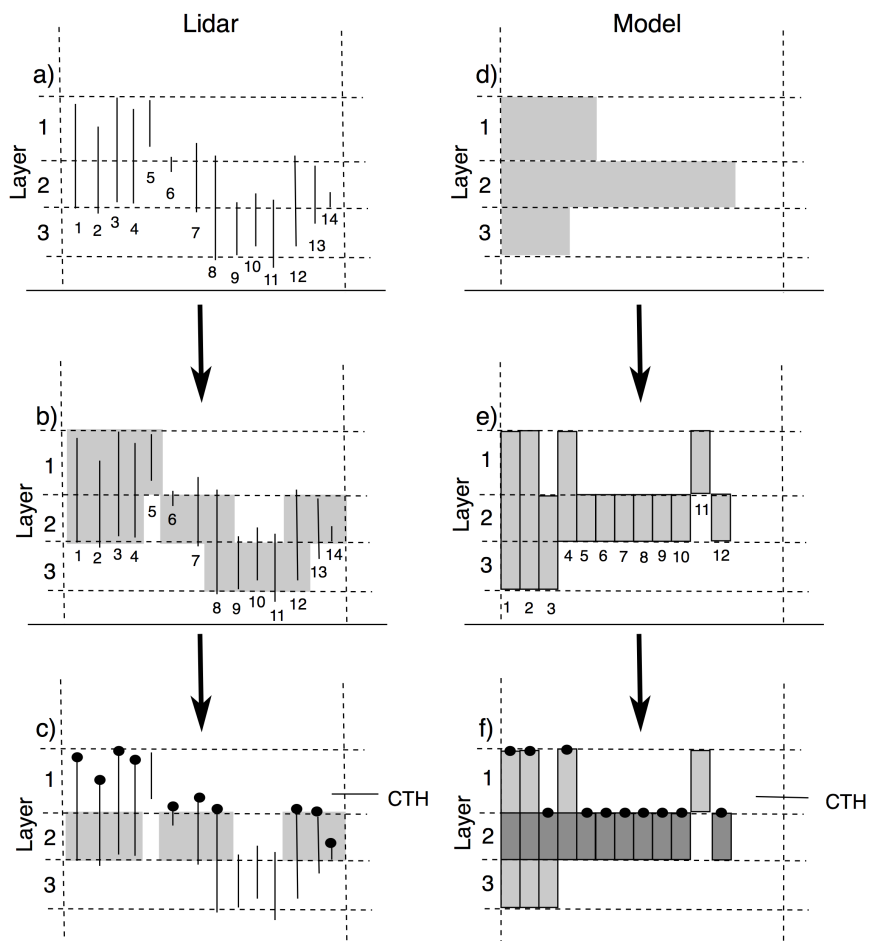
FIG. 3. Schematic illustrating strategy for determining a cloud top height and cloud fraction representative of the boundary layer cloud feature contained within one model grid column. The left columns refers to the method applied to the lidar observations, while the right column refers to the model.
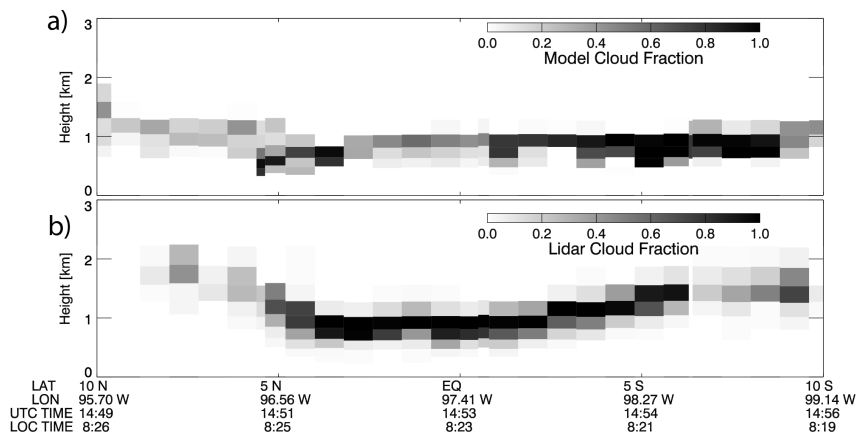
FIG. 4. Panel a) shows the model cloud fraction along the same section of track as shown in 1. Panel b) shows the corresponding lidar-derived cloud fraction.
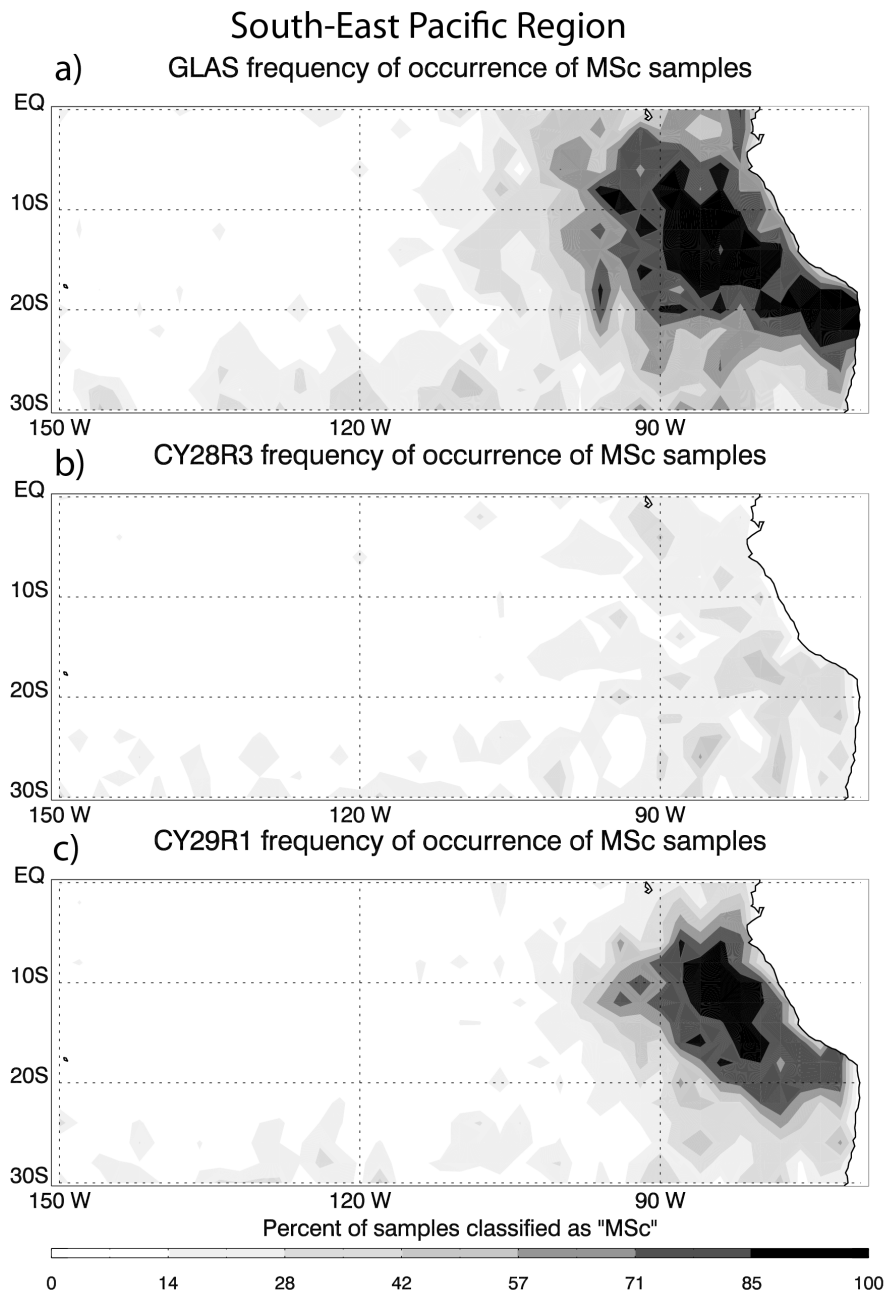
South-East Pacific Region

a) GLAS frequency of occurrence of MSc samples

b) CY28R3 frequency of occurrence of MSc samples

c) CY29R1 frequency of occurrence of MSc samples

Percent of samples classified as "MSc"

0   14   28   42   57   71   85   100

F<small>IG</small>. 5. Frequency of occurrence of MSc samples over the Laser 2A period in the south-east Pacific ocean. Panel a) shows results from the lidar observations, panel b) from the IFS with K-diffusion boundary layer parameterization (CY28R3) and panel c) from the IFS with EDMF parameterization (CY29R1).
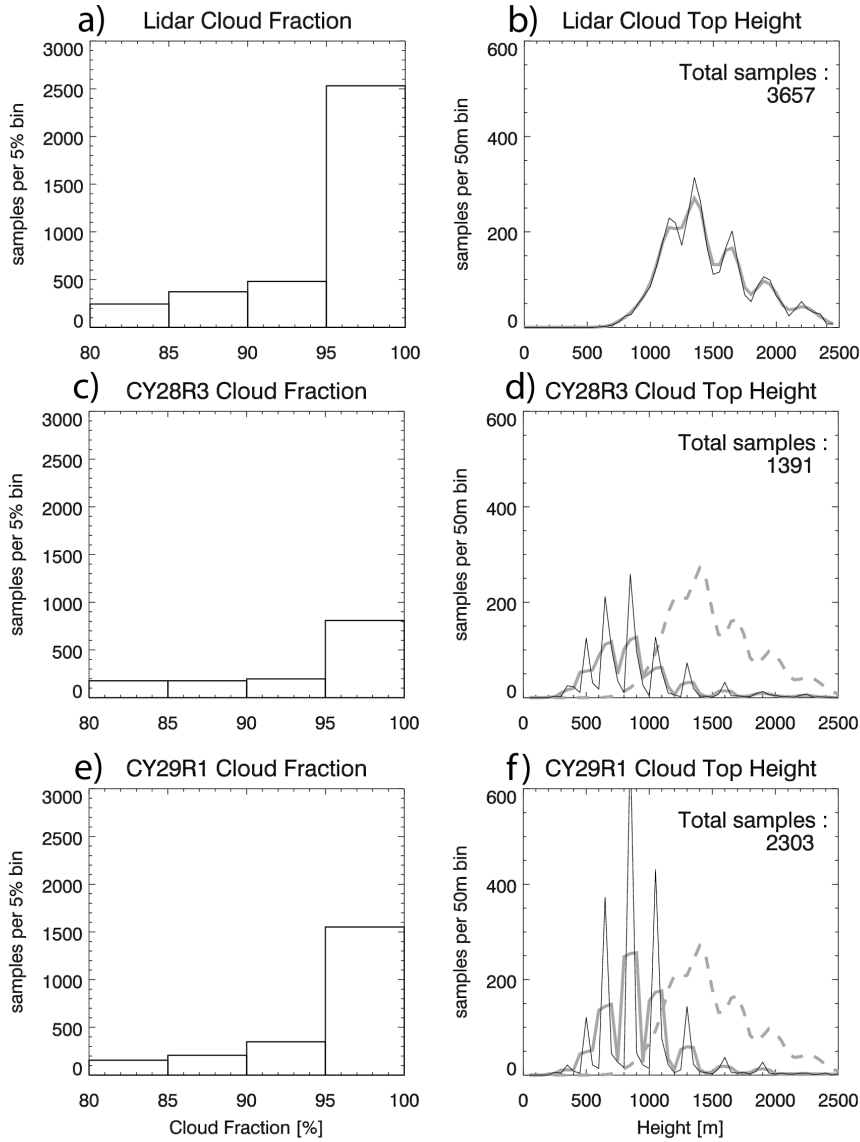
FIG. 6. The left column shows histograms of cloud fraction for all samples identified as MSc. Distributions of cloud top height are shown in the right column. The top row [panels a) and b)] show results from the lidar observations, the middle row [panels c) and d)] from IFS CY28R3 and the bottom row [panels e) and f)] from IFS CY29R1. The thin black curve shows the cloud top height distributions for a 50 m bin size. The thick grey curve is a boxcar running mean over three datapoints. The dashed grey curve in panels d) and f) is the smoothed distribution of lidar cloud tops.

FIG. 7. Same as Fig. 5, with results from the sensitivity test with a more aggressive parcel ascent (CY29R1-E) in panel a) and sensitivity test with less restrictive stability criterion (CY29R1-S) in panel b).
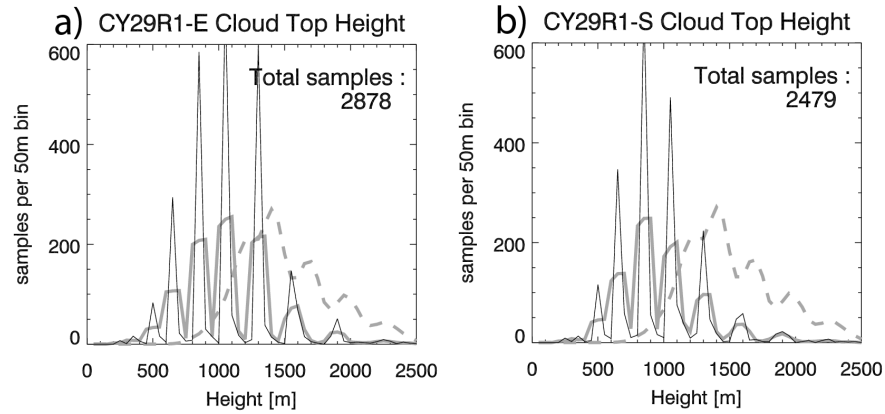
31

FIG. 8. As in Fig. 6. Panel a) shows results from sensitivity test with more aggressive parcel ascent (CY29R1-E) and panel b) shows results from the second sensitivity test with less restrictive stability criterion (CY29R1-S).
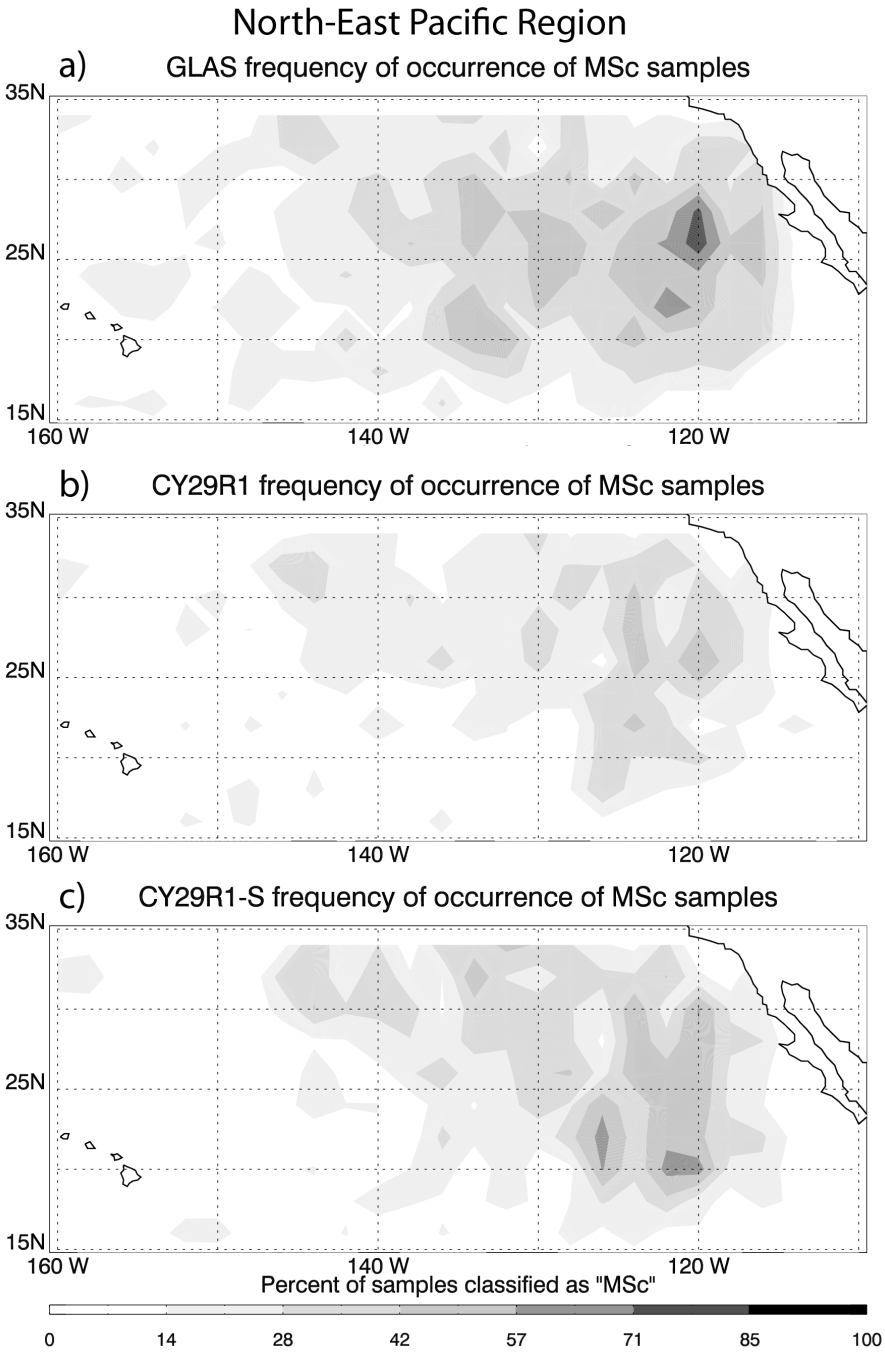
FIG. 9. Frequency of occurrence of MSc samples in the north-east Pacific region. Show in panel a) are results from the observations, in panel b) from the IFS with EDMF parameterization (CY29R1) and in panel c) from the sensitivity run with relaxed lower-level stability criterion (CY29R1-S).
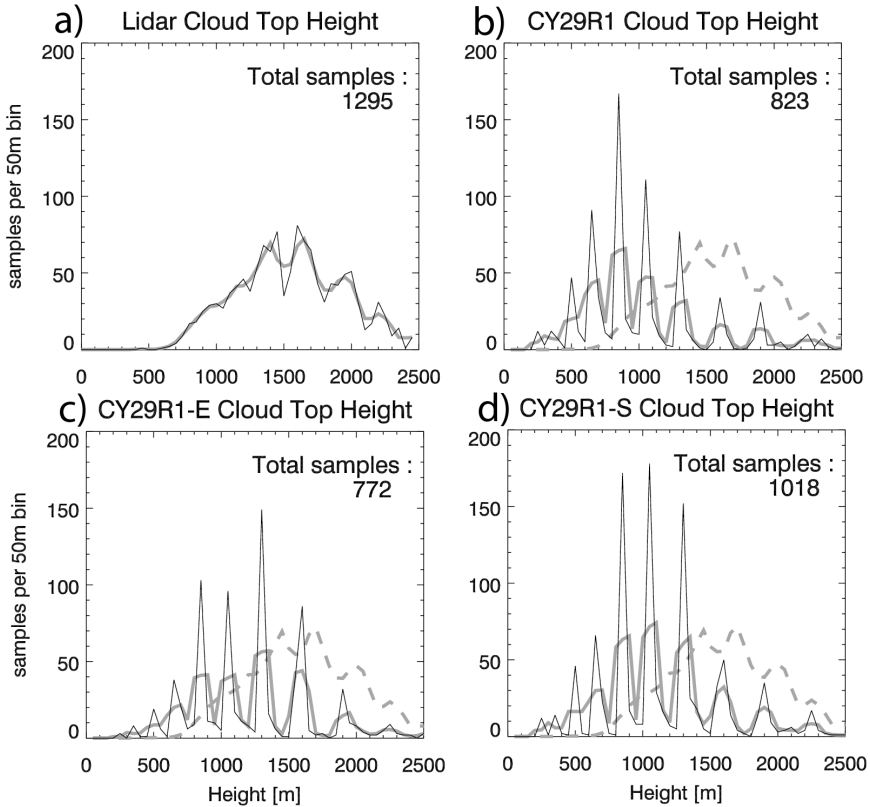
33

North-East Pacific Region

Fig. 10. Cloud top height distributions in the north-east Pacific region for GLAS observations (a), the IFS with EDMF parameterization (b) and the IFS with modified parcel entrainment (c) and stability criterion (d).